Suppressing Influence of Measurement Noise on Vibration-Based Damage Detection Involving Higher-Order Derivatives

Hao Xu, Li Cheng and Zhongqing Su*

The Department of Mechanical Engineering, The Hong Kong Polytechnic University, Kowloon, Hong Kong, China

Abstract: Aimed at minimizing the influence of measurement noise on the precision and robustness of vibration-damage detection (particularly for those approaches involving higher-order derivatives of vibration signals), three independent noise reduction strategies were proposed, including low-pass wavenumber filtering (LWF), adjustment of measurement density (AMD), and hybrid data fusion. Residing on a spectrum analysis, LWF suppresses the noise influence by filtering the measurement noise out of a specific wavenumber domain whilst remaining damage-associated signal features only. AMD is based on an inherent correlation between the degree of noise influence and the density of measurement points. By selecting an optimal AMD, the effect of measurement noise on detection precision can be alleviated. The hybrid data fusion amalgamates signal features acquired under different measurement conditions, giving prominence to the salient features in common (*i.e.*, those pertaining to damage) whereas suppressing less salient features in individuals (*e.g.*, measurement noise and uncertainties). Three proposed noise reduction techniques were validated respectively in simulation, and then applied experimentally to the detection of damage in a plate-like structure under a noisy measurement condition. Satisfactory noise suppression was achieved, demonstrating the effectiveness of the proposed noise reduction strategies for vibration-based damage detection.

Key words: noise reduction, vibration-based damage identification, signal processing.

1. INTRODUCTION

Vibration-based damage detection has been intensively studied in the last two decades. The premise of such a detection philosophy is that the occurrence of damage induces changes in physical properties of the structure under inspection (*e.g.*, local stiffness, density, mass, thermal properties, electric/magnetic conductivity, and electro-mechanical impedance); and these changes are in turn manifested in dynamic responses captured from the structure, *e.g.*, eigen-frequencies (Fan *et al.* 2011; Lee *et al.* 2000; Kim *et al.* 2003). It is understandable that the smaller the damage the more difficult it is to perceive such changes. In order to capture slight changes arising from damage small in size, there is increasing interest in using more sensitive vibration parameters such as changes in mode shape (Mayes 1992) or its derivatives including mode shape curvatures (Pandey *et al.* 1991; Chance *et al.* 1994), strain energy (Stubbs *et al.* 1992) and structural dynamic equilibrium (Xu *et al.* 2011; Cao *et al.* 2012).

It is however envisaged that these sensitive parameters can be prone to the contamination from a variety of interference sources during signal acquisition (*e.g.*, measurement noise and uncertainties, boundary effects and error of finite difference calculation). That is because in most cases the noise in a captured vibration

signal becomes dominant upon a higher-order differentiation, corrupting the high-order derivatives of flexural displacement associated with the damage. Such influence of measurement noise is expected to be severer along with the increase of the derivative order. Thus, it is crucial to develop effective noise reduction techniques so as to enhance the precision and robustness of vibration-based damage detection involving higher-order derivatives.

In the present work, three independent noise reduction strategies were developed, including low-pass wavenumber filtering (LWF), adjustment of measurement density (AMD), and hybrid data fusion. LWF minimizes the noise influence by screening measurement noise from a specific wavenumber domain and remaining damage-associated signal features only; AMD suggests a series of criteria leading to an optimal measurement configuration for striking a balance between the precision of finite difference calculation and noise immunity; and the hybrid data fusion amalgamates signal features acquired under different measurement conditions, highlighting damage-associated signal features and suppressing random measurement noise and uncertainties. Three proposed noise reduction techniques were validated respectively in simulation. To demonstrate their effectiveness and compare individual efficiency, three strategies were respectively applied to a vibration-based damage characterization method based on examining damage-incurred local perturbance to structural dynamic equilibrium.

2. A VIBRATION-BASED DAMAGE DETECTION APPROACH INVOLVING HIGHER-ORDER DERIVATIVES

Without loss of the generality, a vibration-based damage detection approach (Xu *et al.* 2011), by examining damage-incurred local perturbance to structural dynamic equilibrium, was selected to facilitate the understanding and demonstration of the proposed noise reduction strategies.

2.1. Theory

Given a structural component (beam, plate, *etc.*) in its intact status, a certain sort of structural equilibrium based on physical laws must be satisfied. Using a beam component and a plate component for illustration, when the structural component is undergoing steady vibration, one- and two-dimensional damage indices can be established for the beam and the plate components, respectively, defined as,

$$DI = EI \frac{d^4 w(x)}{dx^4} - \rho S \omega^2 w(x) \text{ (for a beam component)} \quad (1)$$

and

$$DI = D \left(\frac{\partial^4 w(x,y)}{\partial x^4} + 2 \frac{\partial^2 w(x,y)}{\partial x^2 \partial y^2} + \frac{\partial^4 w(x,y)}{\partial y^4} \right)$$
$$- \rho h \omega^2 w(x,y). \text{ (for a plate component)} \quad (2)$$

In Eqn 1, $w(x)$ is the flexural displacement of the beam at location x along the beam span when the beam component undergoes a steady vibration with an angular frequency of ω; In the case that the natural excitation is not harmonic, a frequency component in the frequency domain after Fourier transform can also be used. Actually it is preferable to apply this method at off-resonance regime of the structure under inspection, so as to minimize the effect of system damping. The proposed method provides such flexibility in frequency selection. E, ρ, I, and S are the complex modulus of elasticity (comprehending material damping), density, cross-sectional moment of inertia and area of the cross-section for an intact beam, respectively. In Eqn 2, $w(x, y)$ is the flexural displacement of the plate at (x, y); h is the thickness of the plate at (x, y); $D = \dfrac{Eh^3}{12\left(1-\mu^2\right)}$ is the bending stiffness of the plate where μ and E stand for the Poisson's ratio and complex modulus of elasticity, respectively.

In practical manipulation, the damage index can be constructed using the finite difference method. For example, for the two-dimensional *DI*, it has

$$DI_{i,j} = D \left(\chi_{i,j}^{4x} + 2 \chi_{i,j}^{2x2y} + \chi_{i,j}^{4y} \right) + ph_c \omega^2 w_{i,j}, \quad (3)$$

where $w_{i,j}$ is the flexural displacement of the plate measured at point (i, j), and

$$\chi_{i,j}^{4x} = \frac{\partial^4 w}{\partial x^4} = \frac{1}{\Delta_x^4} \times \left(w_{i+2,j} - 4w_{i+1,j} + 6w_{i,j} \right.$$
$$\left. -4w_{i-1,j} + w_{i-2,j} \right), \quad (4a)$$

$$\chi_{i,j}^{4y} = \frac{\partial^4 w}{\partial y^4} = \frac{1}{\Delta_y^4} \times \left(w_{i,j+2} - 4w_{i,j+1} + 6w_{i,j} \right.$$
$$\left. -4w_{i,j-1} + w_{i,j-2} \right), \quad (4b)$$

$$\chi_{i,j}^{2x2y} = \frac{\partial^4 w}{\partial^2 x \partial^2 y} = \frac{1}{\Delta_x^2 \Delta_y^2}$$

$$\times \Big(w_{i+1,j+1} - 2w_{i+1,j} + w_{i+1,j-1} \qquad (4c)$$

$$-2w_{i,j+1} + 4w_{i,j} - 2w_{i,j-1}$$

$$+ w_{i-1,j+1} - 2w_{i-1,j} + w_{i-1,j-1} \Big),$$

where Δ_x and Δ_y are the intervals between two adjacent measurement points along the x– and y– axes, respectively. The high-order derivatives at (i, j) can be obtained in virtue of a finite difference scheme using the displacements measured at its twelve neighboring points, as illustrated in Figure 1, to construct $DI_{i, j}$. It has been demonstrated (Xu *et al*. 2011) that the constructed damage indices present prominent oscillations at the boundaries of a damaged zone, and such an attribute can be utilized to locate and characterize damage precisely in beam and plate components.

2.2. Susceptibility of the Detection Approach to Measurement Noise

However, the above two damage indices involve the fourth-order derivatives of structural vibration deflections $\left(e.g., \dfrac{d^4 w(x)}{dx^4} \text{ and } \dfrac{\partial^4 w(x,y)}{\partial x^4} \right)$. During the fourth-order differentiation, the noise included in $w(x)$ and $w(x, y)$ can be magnified to a significant level, masking damage-induced changes in the damage indices. And thus the robustness of the approach based on Eqns 1 and 2 in practical measurement with noise could be at stake without appropriate de-noising treatment.
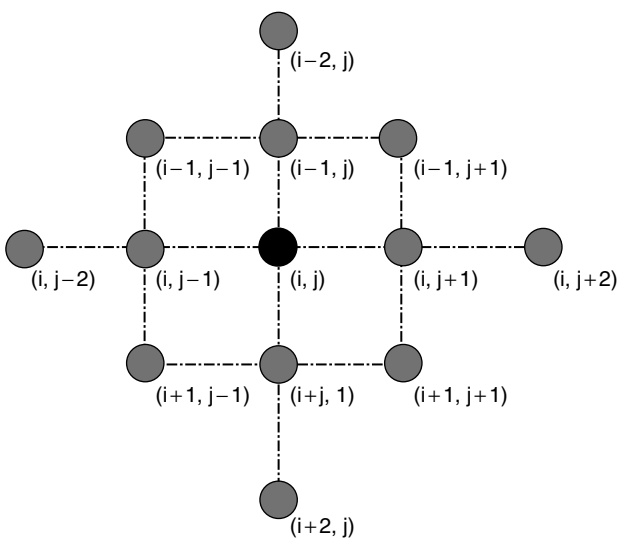
In finite element (FE) simulation, considered a rectangular plate with four simply-supported edges and a damaged zone, as shown in Figure 2. The geometric dimensions and material parameters of the plate are detailed in Table 1. The plate was uniformly meshed with three-dimensional brick elements ($5 \times 5 \times 1$ mm^3 for each), with three layers across the plate thickness. The damaged zone (10×10 mm^2) centered at (310, 230) was simulated by a reduction in the plate thickness by one-third of that in the intact region. A harmonic point force source was applied, to generate a harmonic excitation perpendicular to the plate at 1.1 kHz. To eliminate the singularity near the force source, an inspection region (300×300 mm^2), was defined (in Figure 2). In the inspection region, the flexural displacements, $w_{i, j}$, at all FE nodes on the intact surface of the plate were calculated using the commercial FE code ANSYS®. With them, $DI_{i, j}$ was constructed across the entire inspection region using Eqn 2, exhibited in Figure 3(a). The distribution of $DI_{i, j}$ intuitively indicates the existence, location, rough shape and size of the damaged zone. Note the above results were obtained in the absence of any measurement noise.
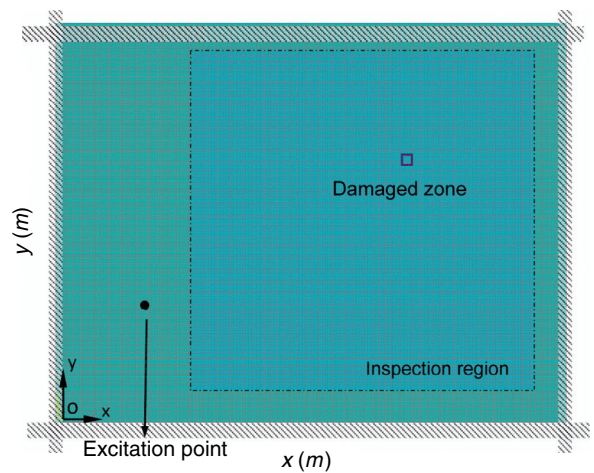

Figure 2. FE model of a rectangular plate with four simply-supported edges and a damaged zone

Figure 1. Measurement points used for constructing the two-dimensional damage index at (i, j)

Table 1. Material properties and geometric parameters of the aluminum plate used in simulation

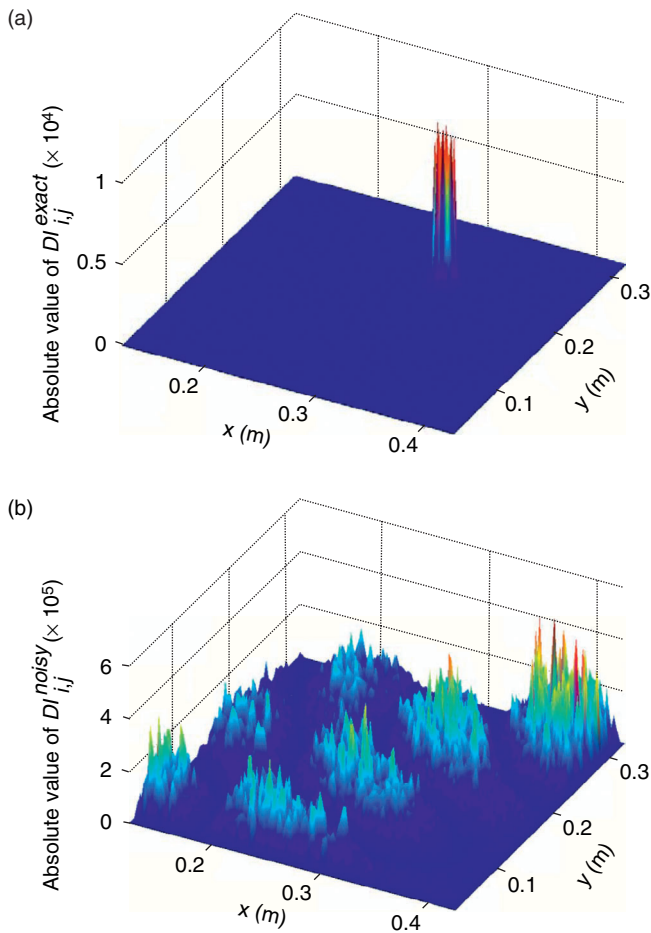|	
Density (kg/m^3)	2700
Young's Modulus E (GPa)	$70 \times (1 + 10^{-3}i)$
Length (mm)	450
Width (mm)	350
Thickness (mm)	3

Figure 3. Constructed $DI_{i,j}$ using (a) noise-free and (b) noise-contaminated nodal displacements at 1.1 kHz

3. DE-NOISING TECHNIQUES

In practical measurement, noise is unavoidable, and the noise influence can be exacerbated for the above approach because the measurement noise can considerably contaminate high-order derivatives of displacement in the constructed damage index during differentiation.

3.1. Introduction of Noise Influence

To introduce noise influence, the calculated nodal flexural displacement was numerically polluted as

$$w_{i,j}^{noisy} = w_{i,j}^{exact} \varepsilon_p + \varepsilon_b, \qquad (5)$$

where

$$\varepsilon_p = \Delta w \cdot e^{j\Delta\varphi} \text{ and } \varepsilon_b = \varepsilon_b^R + j\varepsilon_b^I.$$

In the above, $w_{i,j}^{exact}$ and $w_{i,j}^{noisy}$ represent the flexural displacement at node (i, j) in the absence of any noise and its corresponding noise-polluted counterpart,

respectively; the measurement error, ε_p, is proportional to $w_{i,j}^{exact}$ (where Δw and $\Delta \varphi$ are two Gaussian random real numbers related to the magnitude and phase of $w_{i,j}^{exact}$, respectively); ε_b, the background noise, is constituted by ε_b^R and ε_b^I (another two Gaussian random real numbers associated with real and imaginary parts of the displacement, respectively, to be determined by measurement equipment). The average of Δw was one, and the averages of $\Delta\varphi$, ε_b^R and ε_b^I were all assumed to be zero, and their corresponding standard derivations are: $\sigma\{\Delta w\} = 1\%$, $\sigma\{\Delta\varphi\} = 1°$ and $\sigma\{\varepsilon_b^R\} = \sigma\{\varepsilon_b^I\} = 10^{-10}\,\text{m}$.

With all other parameters in simulation remained unchanged, the constructed damage index using $w_{i,j}^{noisy}$ (denoted by $DI_{i,j}^{noisy}$) is shown in Figure 3(b) for the damaged plate in Figure 2. It can be seen that, as a result of the interference from the added measurement noise, recognition of signal features associated with damage becomes intractable, and the measurement noise, even tiny (only 1% in this example), was magnified significantly during the fourth-order differentiation. The high susceptibility of the detection approach to measurement noise entails effective de-noising treatments.

To minimize the influence of measurement noise, three independent de-noising techniques were developed: *Low-pass Wavenumber Filtering* (LWF), *Adjustment of Measurement Density* (AMD) and hybrid data fusion.

3.2. Low-Pass Wavenumber Filtering (LWF)

LWF is a post-processing treatment for de-noising based on the spectrum analysis. By way of illustration, Figure 4 shows the spectra of $DI_{i,j}^{exact}$ [in Figure 3(a)] and $DI_{i,j}^{noisy}$ [in Figure 3(b)] obtained using the two-dimensional Fast Fourier Transform (FFT). It can be observed that the majority of wavenumbers of $DI_{i,j}^{exact}$ are concentrated in a relatively low wavenumber region [Figure 4(a)], whereas the noise influence is prevailing in a relatively high wavenumber region [Figure 4(b)]. By letting $k_y = 0$, $DI_{i,j}^{exact}$ and $DI_{i,j}^{noisy}$ in the wavenumber domain were co-presented in Figure 4(c), showing an overlap in between when $-k_c < k_x < k_c$, where k_x is the wavenumber in x–axis. The same observation was obtained when $k_x = 0$ and $-k_c < k_y < k_c$ (where k_y is the wavenumber in y–axis). Based on the above, a low-pass filtering function was designed to screen out the noise interference in the high wavenumber region, defined as

$$\tilde{h}(k_x, k_y) = \begin{cases} 1 & \text{when } \left(|k_x| \le k_c \text{ and } |k_y| \le k_c\right) \\ 0 & \text{otherwise,} \end{cases} \qquad (6)$$
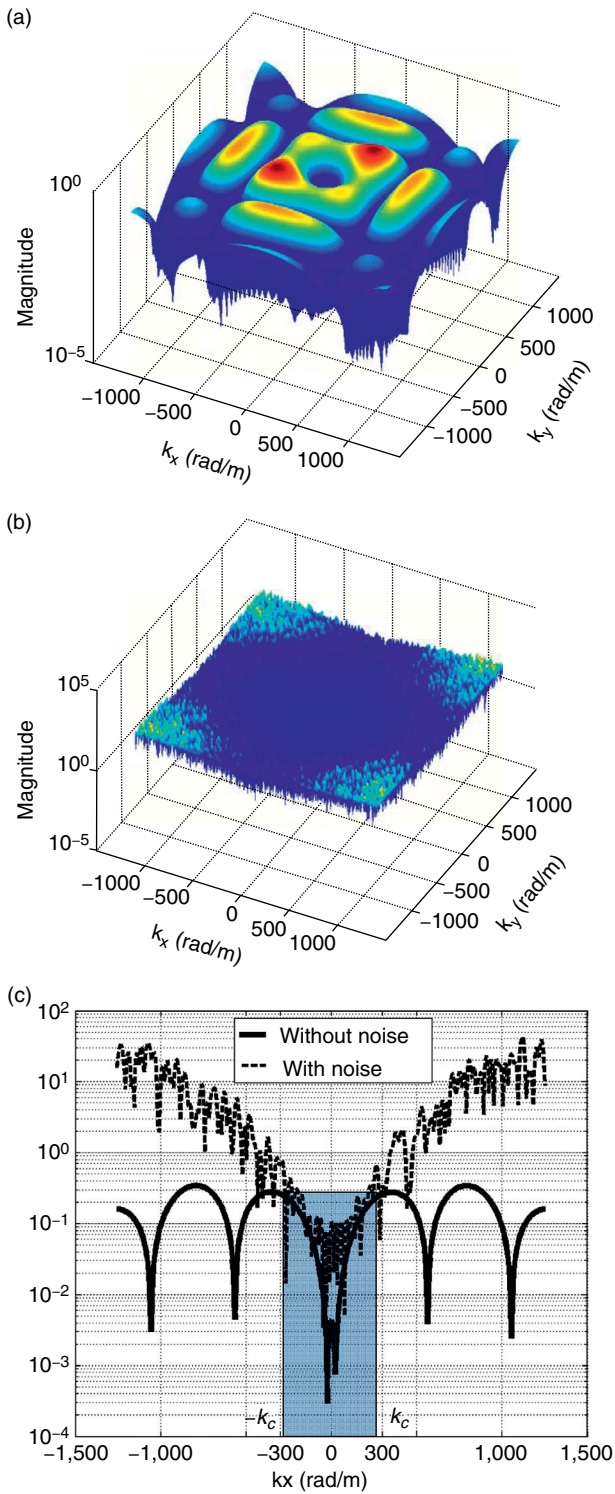
Figure 4. Two-dimensional FFT analysis for (a) noise-free and (b) noise-contaminated $DI_{i,j}$ in Figure 3; and (c) combined presentation of (a) and (b) when $k_y = 0$

process of low-pass filtering, the residual signal features can be re-constructed to the spatial domain using the inverse two-dimensional FFT.

For the above discussed damaged plate, $DI_{i,j}^{exact}$ and $DI_{i,j}^{noisy}$ shared an overlap range of (−300, 300) in the wavenumber domain as seen in Figure 4(c), and therefore a cutoff wavenumber, $k_c = 300$ rad/m, was selected. It is noteworthy that the cutoff wavenumber was selected based on a 'trial-and-error' principle, and there is no a universal criterion applicable to all the cases. The selection is substantially subject to damage location, severity, excitation frequency and the density of measurement points. Applied with LWF, the re-constructed $DI_{i,j}^{exact}$ and $DI_{i,j}^{noisy}$ using inverse two-dimensional FFT are shown in Figures 5(a) and (b), respectively, revealing an apparently enhanced precision compared with the originals in Figure 3, highlighting not only the location of the damaged zone but also its approximate size, even under the interference of measurement noise [Figure 5(b)].
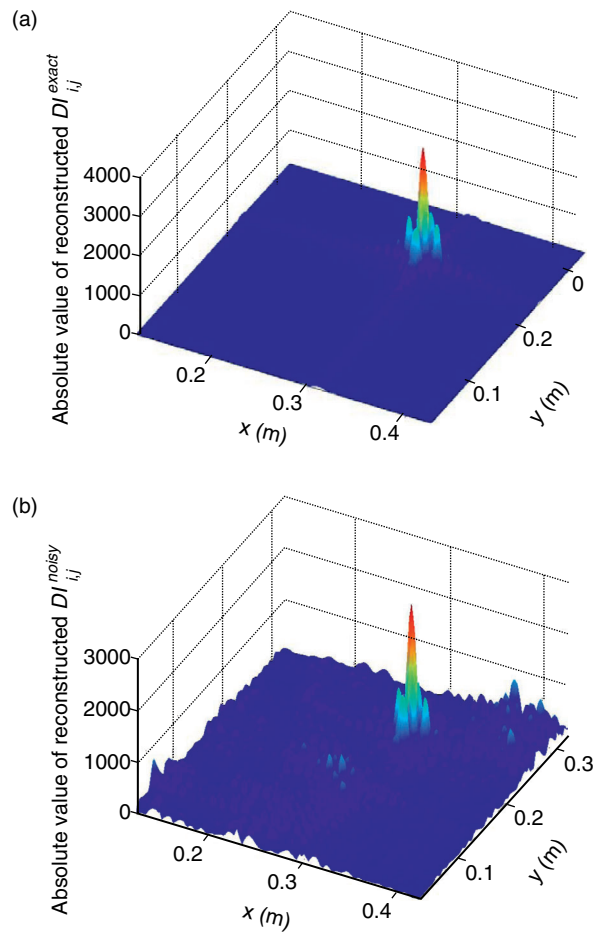

Figure 5. Re-constructed (a) noise-free and (b) noise-contaminated $DI_{i,j}$ via inverse two-dimensional FFT ($k_c = 300$ rad/m)

where k_c is the cutoff wavenumber with a unit of rad m^{-1}. Similar to a Heaviside function (Xu *et al.* 2011), Eqn 6 eliminates signal features outside of the range where $DI_{i,j}^{exact}$ and $DI_{i,j}^{noisy}$ overlap. After the

3.3. Adjustment of Measurement Density (AMD)

AMD was developed as an alternative to reduce the noise influence, based on an inherent correlation among the accuracy of finite difference calculation, the extent of noise influence, and the density of measurement points (represented by the distances between two adjacent measurement points, d_m, corresponding to the differential interval Δ_x or Δ_y in the finite difference in Eqn 4). Specifically speaking, along with the increase of d_m, the accuracy of finite difference calculation decreases due to the strengthening truncation errors; whereas at the same time the noise interference is alleviated, giving rise to the enhanced noise immunity; and *vice versa*. Thus an optimal selection of d_m can reach a compromise between the accuracy of finite difference calculation and noise immunity. For discussion, a dimensionless parameter, d_m/λ, was established where λ, the structural vibration wavelength, was chosen to be the wavelength of an infinite plate undergoing a free harmonic vibration, as (Hagedorn *et al.* 2007)

$$\lambda = \frac{2\pi}{k} , \qquad (7)$$

where wavenumber $k = \sqrt[4]{\dfrac{\rho h \omega^2}{D}}$. The constructed $DI_{i,j}^{exact}$ and $DI_{i,j}^{noisy}$ for the above discussed damaged plate at four different d_m/λ (0.046, 0.092, 0.123 and 0.185) are compared in Figure 6. It can be observed that, as d_m/λ increases, the accuracy of characterization reduces ($DI_{i,j}^{exact}$ and $DI_{i,j}^{noisy}$ progressively lose the capabilities of locating the damage), whereas along with an enhanced immunity of measurement noise ($DI_{i,j}^{exact}$ coincides with $DI_{i,j}^{noisy}$ more). In particular, d_m/λ = 0.123 [Figures 6(e) and (f)], corresponding to the case with roughly eight measurement points per wavelength, can be regarded as an optimal configuration of measurement.

Furthermore, two normalized signal parameters, AD (*Accuracy of finite Difference*) and NI (*Noise Influence*), were introduced to facilitate the optimal selection of d_m/λ.

3.3.1. Accuracy of difference (AD)

An *equivalent estimation region* (EER) was specified, as highlighted in Figure 7(a). The size of EER is in general larger than the actual damaged zone, to embrace all the peaks of $DI_{i,j}^{exact}$ at the boundary of the damaged zone. The maximum peak values of $DI_{i,j}^{exact}$ within and outside of the EER are denoted as c and t, respectively

[as shown in Figure 7(b)], and r is defined to be the ratio of t/c, then AD is defined as

$$AD = \frac{r}{r_c} = \frac{t}{c \cdot r_c} , \qquad (8)$$

where r_c is a threshold. r depicts the degree of damage-introduced protrusion of $DI_{i,j}^{exact}$ within and outside of EER, accordingly reflecting the accuracy of damage characterization. Provided r is greater than r_c (*i.e.*, AD > 1), the accuracy is deemed unacceptable, and *vice versa*. In other words, the accuracy is satisfactory only within the range of [0, 1].

3.3.2. Noise influence (NI)

NI was defined in terms of the quantitative similarity between $DI_{i,j}^{exact}$ and $DI_{i,j}^{noisy}$ at a specific spatial location, calibrated using a two-dimensional correlation coefficient Ξ, given by

$$\Xi = \frac{N \sum_{i=1}^{N_y} \sum_{j=1}^{N_x} DI_{i,j}^{exact} DI_{i,j}^{noisy} - \sum_{i=1}^{N_y} \sum_{j=1}^{N_x} DI_{i,j}^{exact} \sum_{i=1}^{N_y} \sum_{j=1}^{N_x} DI_{i,j}^{noisy}}{\sqrt{N \sum_{i=1}^{N_y} \sum_{j=1}^{N_x} \left(DI_{i,j}^{exact}\right)^2 - \left(\sum_{i=1}^{N_y} \sum_{j=1}^{N_x} DI_{i,j}^{exact}\right)^2} \cdot \sqrt{N \sum_{i=1}^{N_y} \sum_{j=1}^{N_x} \left(DI_{i,j}^{noisy}\right)^2 - \left(\sum_{i=1}^{N_y} \sum_{j=1}^{N_x} DI_{i,j}^{noisy}\right)^2}}$$

$$(9)$$

where N_x and N_y denote the number of measurement points along $x-$ and $y-$ axes, respectively. Ξ varies in the range of [0, 1], and the unity of Ξ ($\Xi = 1$) indicates a perfect matching between $DI_{i,j}^{exact}$ and $DI_{i,j}^{noisy}$ (*i.e.*, ideal case without any noise interference). A threshold Ξ_c can be defined to judge the acceptability of noise interference, with which NI is given by

$$NI = \frac{1 - \Xi}{1 - \Xi_c} . \qquad (10)$$

Provided Ξ is less than Ξ_c (i.e., NI > 1, meaning a poor similarity between $DI_{i,j}^{exact}$ and $DI_{i,j}^{noisy}$), the interference of noise is unacceptable. An acceptable NI should be within the range of [0, 1].

It can thus be seen that a balance between the accuracy of finite difference calculation and noise immunity can be achieved when both *AD* and *NI* concurrently fall in the range of [0, 1], and such a range is called '*acceptable region*'. Figure 8 displays *AD* and *NI* distributions when d_m/λ = 0.016, 0.031, 0.046, 0.062, 0.076, 0.092, 0.123, 0.154, 0.185, respectively. Such a concurrent presentation of both *AD* and *NI* distribution is called '*AD-NI curve*' in this study. The intersection between *AD* and *NI* curves, p_o in Figure 8, can be regarded as the most optimal selection of d_m/λ. That is
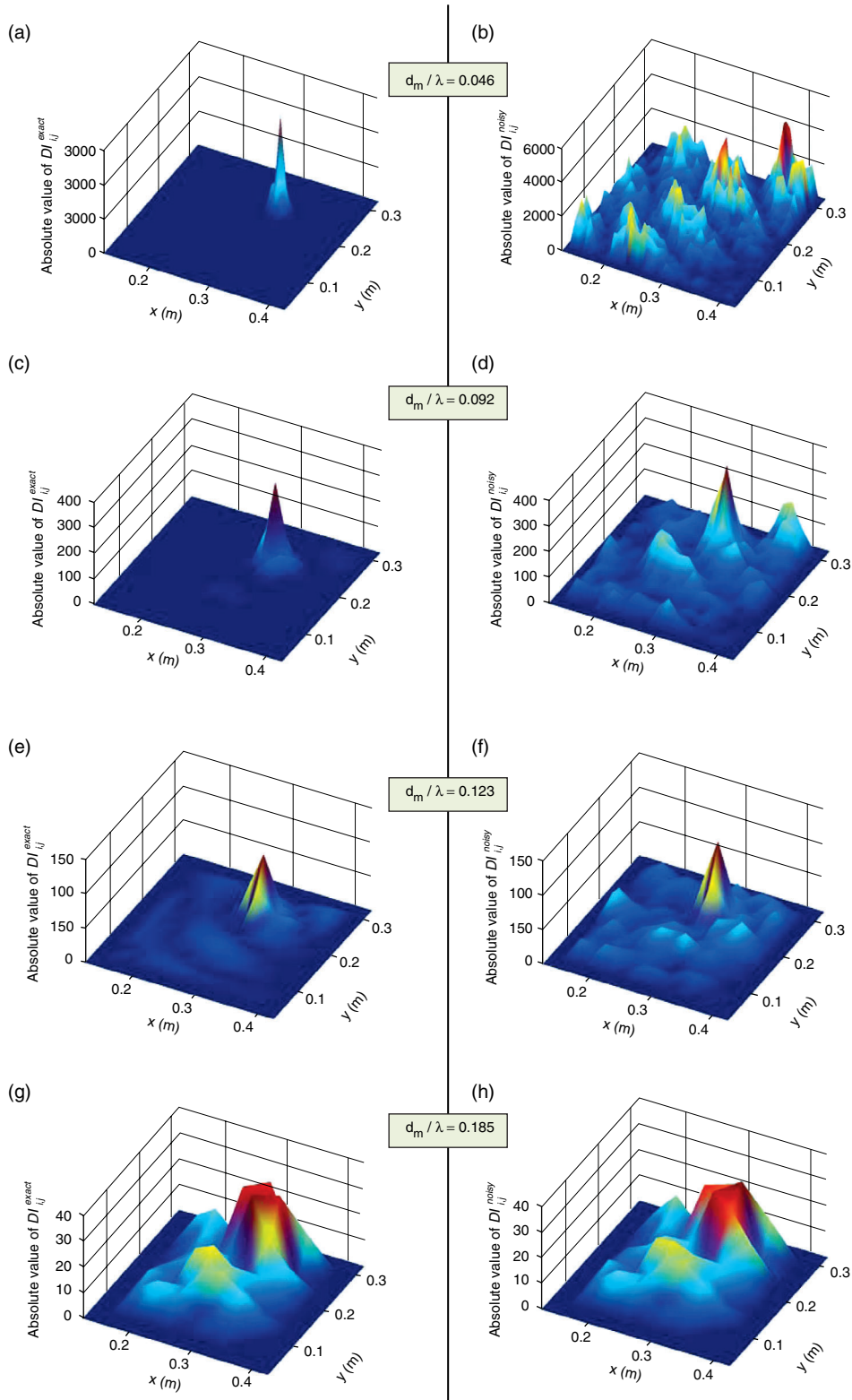
Figure 6. Constructed $DI_{i,j}$ using noise-free nodal displacements (left column) and using noise-contaminated nodal displacements (right column) at different d_m/λ

because the position of the current p_o warrants that both *AD* and *NI* are in the acceptable region [0, 1] concurrently, meeting the above criterion for the determination of *AD* and *NI*. It is also interesting to observe that the recommended measurement configuration ($d_m/\lambda = 0.123$) previously determined
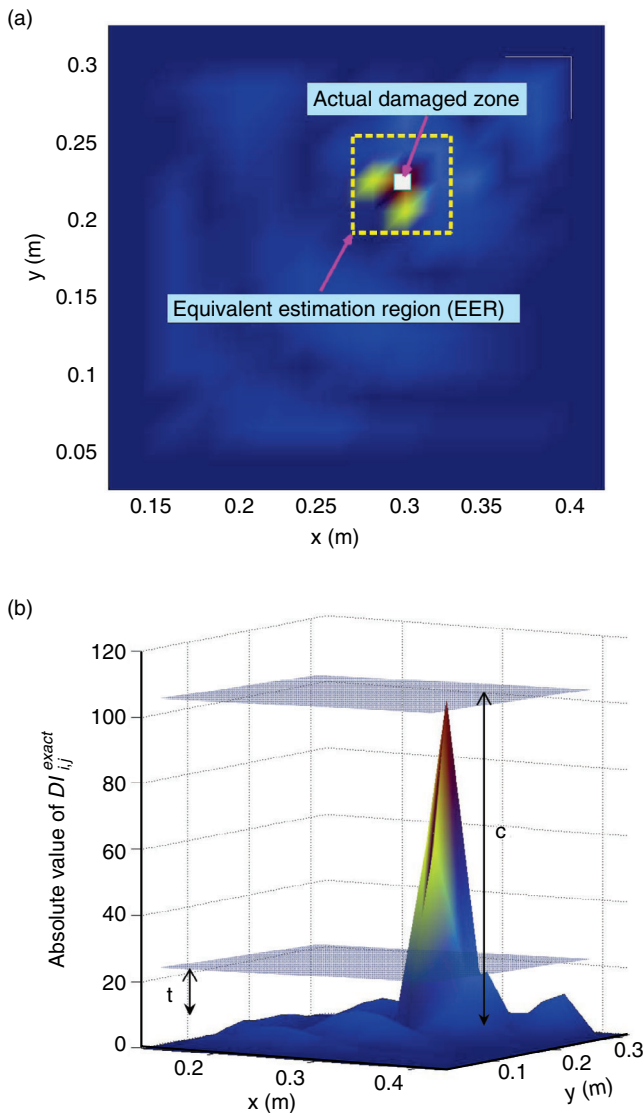
(a)

(b)

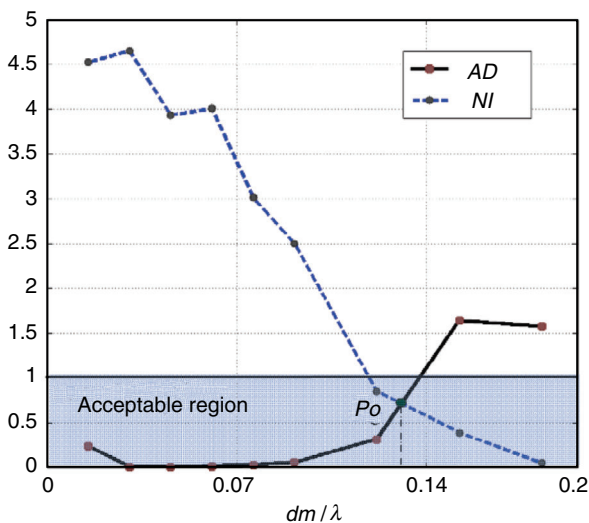**Figure 7.** Illustration for defining (a) equivalent estimation region (EER); and (b) signal parameter *AD*

Figure 8. Variation in *AD* and *NI* for the plate in Figure 2 at different d_m/λ ($r_c = 0.4$, $\Xi_c = 0.8$)

from Figures 6(e) and 6(f) is close to p_o. In contrast, other options of d_m/λ give rise to either poor accuracy of finite difference calculation [*e.g.*, $d_m/\lambda = 0.185$, in Figure 6(h)] or weak noise immunity [*e.g.*, $d_m/\lambda = 0.046$ in Figure 6(b)].

3.4. Hybrid Data Fusion

In the detection approach, $DI_{i,j}$ can be constructed under a variety of measurement conditions (*e.g.*, under different excitation frequencies and measurement densities, processed by LWF or AMD method), rendering a number of $DI_{i,j}$ distribution maps (for example, those in Figure 6). A hybrid data fusion algorithm was developed to further suppress the influence of measurement noise. Assuming at the same position (i, j), $DI_{i,j}$ can be obtained under K different measurement circumstances, denoted by $DI_{i,j-1}$, $DI_{i,j-2}$, $DI_{i,j-L}$, …, $DI_{i,j-L}$, $DI_{i,j-K}$ ($L = 1, 2, L, K$), the hybrid fusion algorithm is defined as (Su *et al.* 2009a; Su *et al.* 2009b; Ihn *et al.* 2008; Lu *et al.* 2010)

$$DI_{i,j\text{-}hybrid} = DI_{i,j\text{-}arithmetic} \cap DI_{i,j\text{-}geometric}, \quad (11a)$$

where

$$DI_{i,j\text{-}arithmetic} = \frac{1}{K}\sum_{L=1}^{K} DI_{i,j-L}, \quad (11b)$$

and

$$DI_{i,j\text{-}geometric}$$
$$= \sqrt[K]{DI_{i-1} \cdot DI_{i,j-2} \cdot \ldots DI_{i,j-L} \cdots DI_{i,j-K}}. \quad (11c)$$

$DI_{i,j\text{-}hybrid}$ is the ultimate fused value at (i, j) upon fusion. The arithmetic mean takes into account all information sources, and the signal features associated with damage and measurement noise are all included. Such an averaging manner accumulates the noise influence, and the local protrusion of damage-related features may become less prominent. In contrast, the geometric mean highlights the common features only in all sources, therefore capable of reducing random noise influence and eliminating false alarms. But it may lower the likelihood of damage presence because it multiplicatively processes all sources, and any low possibility in a particular source can lead to a considerably low likelihood in the fused map. Thus, the hybrid fusion, in Eqn 11(a), can be seen as an optimal option as it well achieves a compromise between the arithmetic and geometric fusions, to give prominence to the salient features pertaining to damage and suppress the noise influence at the same time.

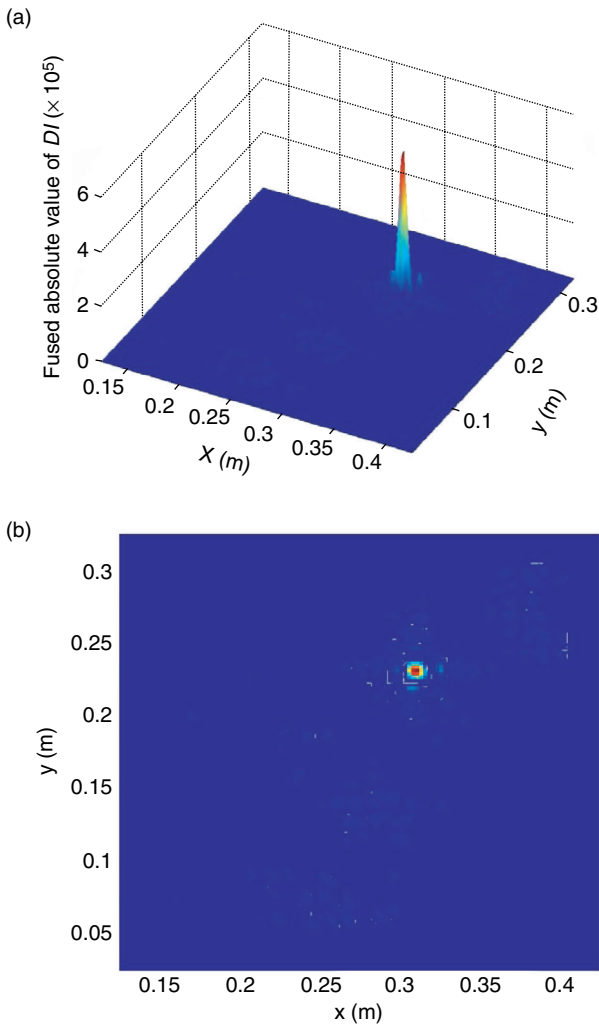Figure 9 presents the two- and three-dimensional fused map using the constructed damage index from

(a)

(b)

Figure 9. (a) Three- and (b) two-dimensional presentations of the fused map using the constructed damage index from two sources [the noise-polluted source image in Figure 3(b) treated with LWF and the one in Figure 6(f)]
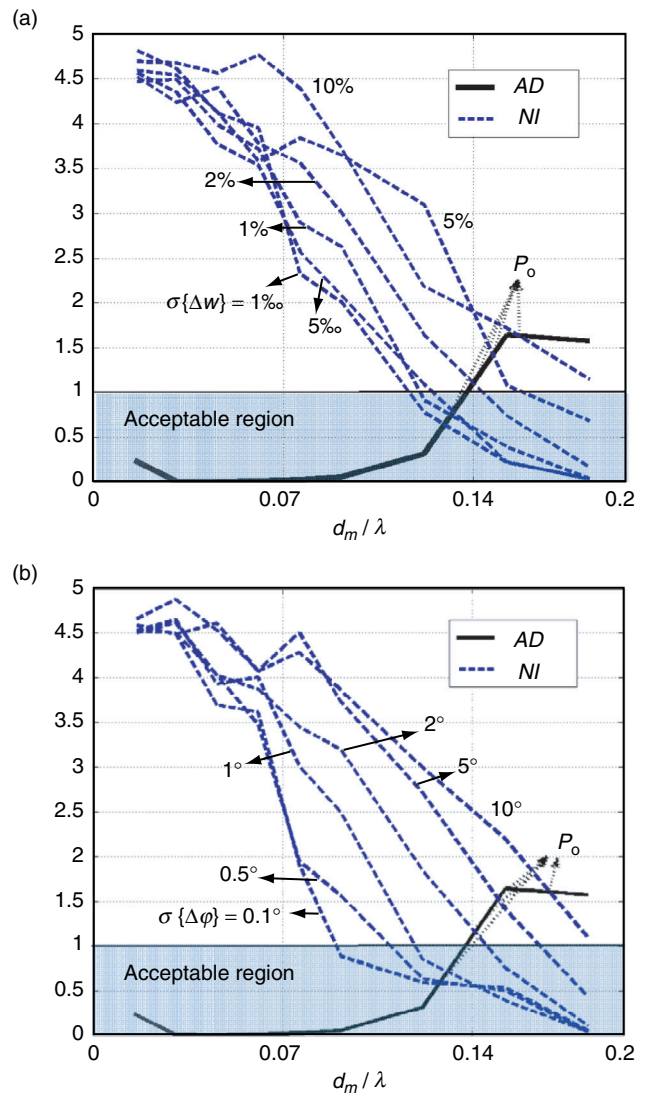
(a)

(b)

Figure 10. Variation in AD-NI curves for the plate in Figure 2 along with increasing measurement errors in (a) noise magnitudes and (b) noise phases ($r_c = 0.4$, $\Xi_c = 0.8$)

two sources [the noise-polluted source image in Figure 3(b) treated with LWF and the one in Figure 6(f)]. Although two information sources were fused only, considerably enhanced detection precision has been achieved, to see that the fused results outperform either sources in predicting the location and shape of the damaged zone.

4. DISCUSSION

Keeping the averages of ε_b^R and ε_b^I to be zero and $\sigma\left\{\varepsilon_b^R\right\} = \sigma\left\{\varepsilon_b^I\right\} = 10^{-10}\,\text{m}$ in the background noise in Eqn 5, Figure 10 exhibits the variation of AD-NI curves subject to different $\sigma\{\Delta w\}$ (from 1‰ to 10%) when $\sigma\{\Delta\varphi\} = 1°$ [Figure 10(a)], and different $\sigma\{\Delta\varphi\}$ (from 0.1° to 10º) when $\sigma\{\Delta w\} = 1\%$ [Figure 10(b)], respectively. The increasing level of simulated measurement noise is observed to shift the *NI* curve

upwards, and thus the position of p_o is elevated in the acceptable region, leading to a reduced flexibility in selecting optimal measurement density. A greater noise level requests larger d_m/λ (*i.e.*, sparser measurement density) to suppress the noise influence, but doing this will apparently sacrifice the accuracy of the finite difference calculation. From the observations in Figure 10, 0.08~0.13 for d_m/λ (corresponding to eight ~ thirteen measurement points per λ) could be an optimal configuration. On the other hand, with less noise, p_o moves towards a smaller d_m/λ at which more measurement points can be arranged. Generally speaking, a selection of around ten measurement points per wavelength could be proposed as a rule of thumb for ascertaining an optimal measurement configuration.

5. APPLICATION

As an application, the above proposed de-noising techniques were employed to suppress the influence of measurement noise on the vibration-based damage characterization method detailed in Section 2. As shown in Figure 11(a), a rectangular aluminum plate was prepared (Young's Modulus: $E = 70 \times (1 + 10^{-2}i)$ *GPa*, density: 2700 kg/m³; 450 mm long, 410 mm wide and 3 mm thick) with clamped right and lower edges. Another two pieces of aluminum plates with randomly selected shapes were fastened to the upper and left edges of the plate using bolts [Figure 11(b)] to introduce complex boundary conditions purposely. A damaged zone with a cross-like shape was introduced to the plate by milling the plate with a 1 mm reduction in its thickness, with its centre 282 mm and 257.5 mm away from the left and lower edges of the plate, respectively, as seen in Figure 11(b). The specific dimension of the damaged zone is shown in Figure 11(c). A shaker (B&K 4809), driven by an excitation at 1.51 kHz, was in contact with the plate surface bearing the damage, at the point 123 mm and 95 mm away from the left and lower edges, respectively. To exclude the excitation point, an inspection region was selected 85~409 mm to the left edge and 114~429 mm to the lower edge. The inspection region was meshed evenly using 73 × 73 measurement points, at each of which the displacement was captured using a scanning laser interferometry system (Polytec® Scanning Vibrometer, PSV-400) from the intact plate surface (*i.e.*, the plate surface free of the damage and the excitation source).

The constructed $DI_{i,j}$ using the raw displacement signal without any signal de-noising treatment is shown in Figure 12(a), providing no straightforward information to describe the damage due to the severe noise influence. LWF was first applied. With a cutoff wavenumber of 200 rad/m, the re-constructed $DI_{i,j}$ over the inspection region is shown in Figure 12(b), highlighting the position of the damaged zone with much reduced noise influence. Then AMD was applied independently, by reducing the number of measurement points from 73 × 73 to 19 × 19 (corresponding to $d_m/\lambda = 0.13$, *viz.*, around eight measurement points per wavelength, as suggested in Section 3.3), and the detection results are shown in Figure 12(c), depicting roughly the location and size of the damaged zone. Subsequently, two images obtained using LWF and AMD, respectively, were processed with the hybrid data fusion algorithm, and the fused results are presented in Figure 12(d), in which the damage location and rough size become more explicit, compared with individual images shown in Figures 12(b) and 12(c), demonstrating the
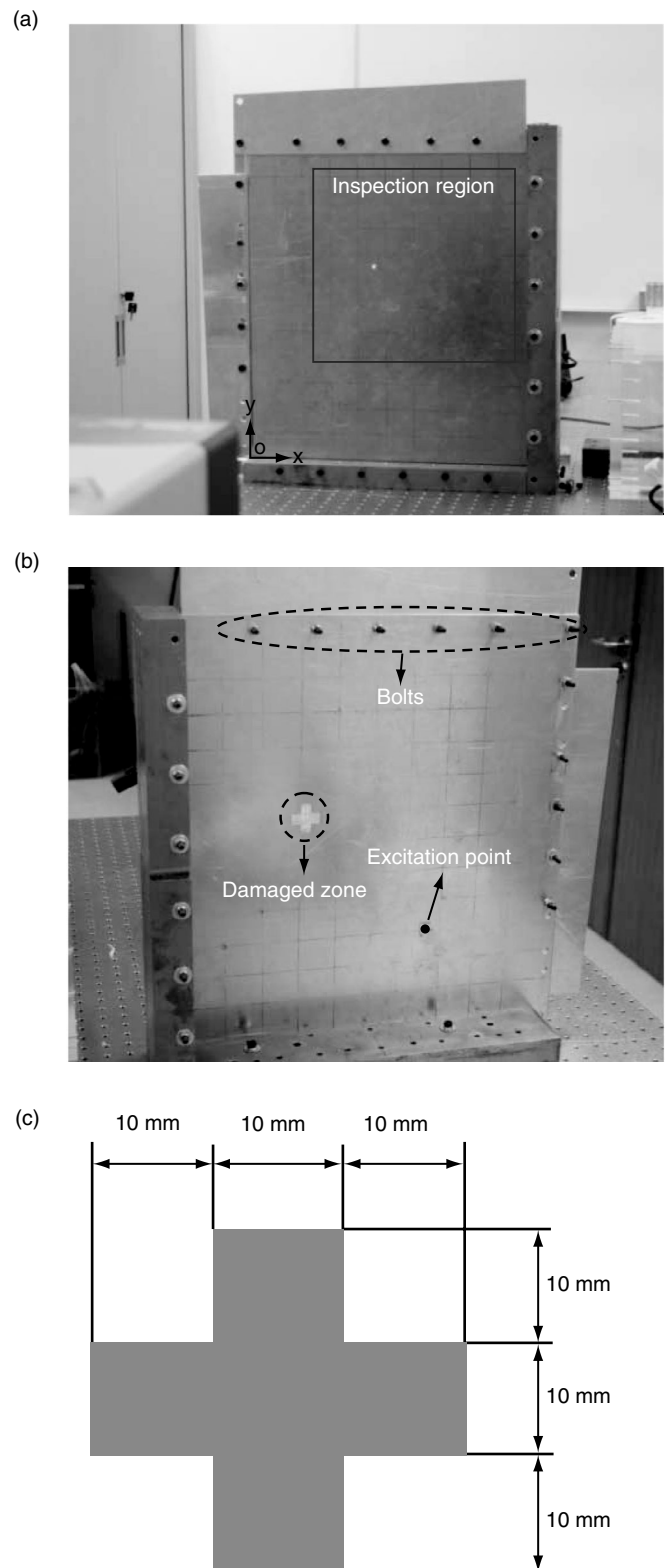
(a)

(b)

(c)

Figure 11. An aluminum structural system containing a damaged zone for application of the proposed de-noising approaches: (a) front and (b) back view; and (c) specific dimension of the damaged zone

improved noise immunity of the approach when three de-noising techniques were used simultaneously.
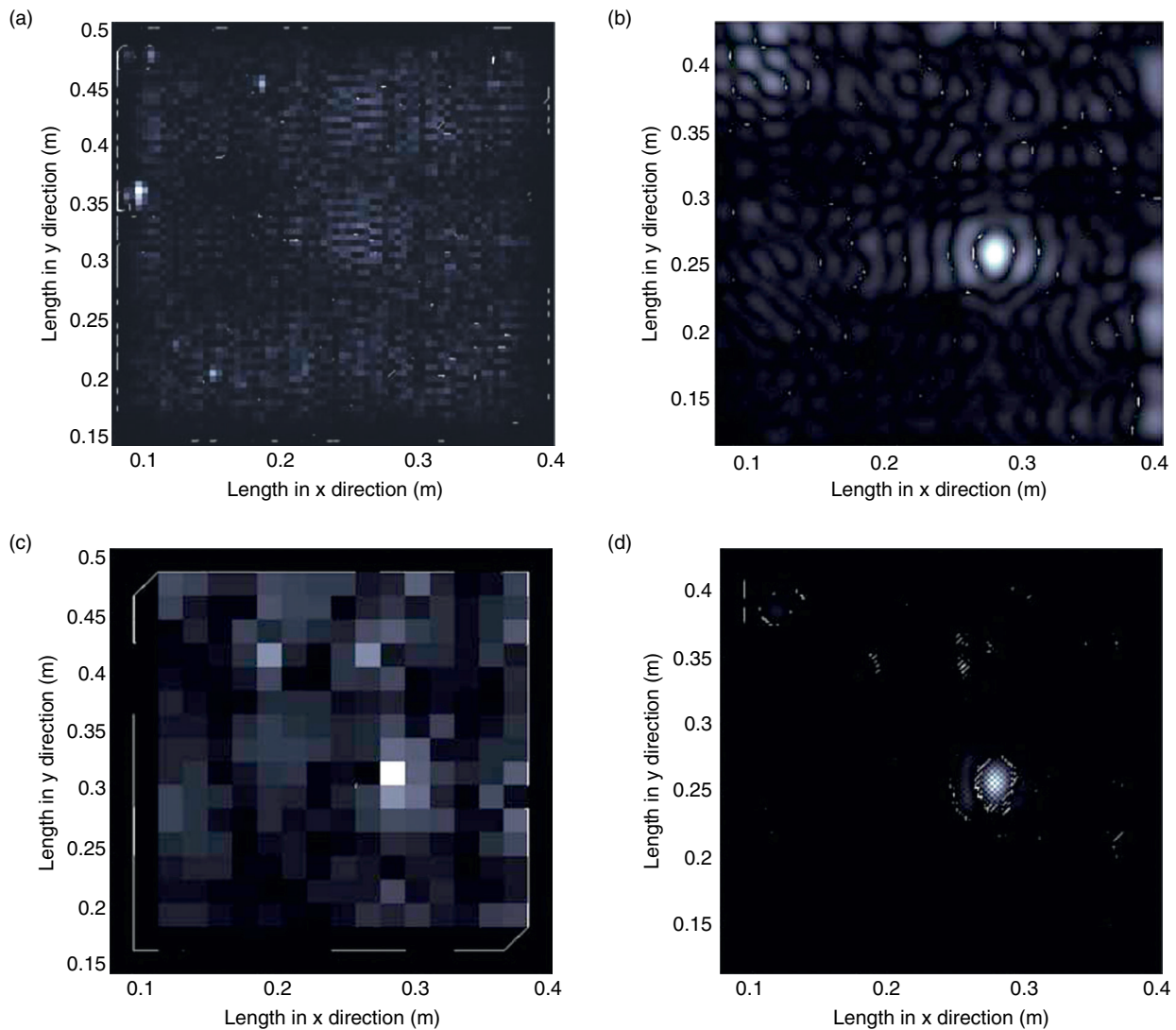
Figure 12. Constructed $DI_{i,j}$ for the structural system in Figure 11: (a) without any de-noising treatment; (b) treated with LWF; (c) treated with AMD; and (d) treated with hybrid data fusion

6. CONCLUSION

Three de-noising approaches were proposed with a purpose of reducing the influence of measurement noise on the precision and robustness of vibration-based damage detection involving higher-order derivatives of vibration signals, including low-pass wavenumber filtering (LWF), adjustment of measurement density (AMD), and hybrid data fusion. The LWF has proven effectiveness in minimizing measurement noise by selecting an appropriate cutoff wavenumber to remain damage-associated signal features in lower wavenumber domain. As a rule of thumb, ten measurement points per wavelength could be an optimal selection towards reduced effect of measurement noise and a balance between detection accuracy and noise immunity. The hybrid data fusion provides further enhanced tolerance to measurement noise by standing out signal features pertaining to damage while suppressing random measurement noise and uncertainties. Three proposed noise reduction techniques were applied to reduce the noise influence on a vibration-based damage detection exercise, and satisfactory noise suppression was achieved, demonstrating the effectiveness of the proposed noise reduction strategies for vibration-based damage detection.

REFERENCES
Cao, M., Cheng, L., Su, Z. and Xu, H. (2012). "A multi-scale pseudo-force model in wavelet domain for identification of damage in structural components", *Mechanical Systems and Signal Processing*, Vol. 28, pp. 638–659.

Chance, J., Tomlinson, G.R. and Worden, K. (1994). "A simplified approach to the numerical and experimental modeling of the dynamics of a cracked beam", *Proceedings of the Twelfth International Modal Analysis Conference*, Honolulu, Hawaii, USA, pp. 778–785.

Fan, W. and Qiao, P. (2011). "Vibration-based damage identification methods: a review and comparative study", *Structural Health Monitoring*, Vol. 10, No. 1, pp. 83–111.

Hagedorn, P. and DasGupta, A. (2007). *Vibrations and Waves in Continuous Mechanical Systems*, John Wiley & Sons Ltd, Chichester, UK.

Ihn, J.B. and Chang, F.K. (2008). "Pitch-catch active sensing methods in structural health monitoring for aircraft structures", *Structural Health Monitoring*, Vol. 7, No. 1, pp. 5–15.

Kim, J.T., Ryu, Y.S., Cho, H.M. and Stubbs, N. (2003). "Damage identification in beam-type structures: frequency-based method vs. mode-shape-based method", *Engineering Structures*, Vol. 25, No. 1, pp. 57–67.

Lee, Y.S. and Chung, M.J. (2000). "A study on crack detection using eigen-frequency test data", *Computers and Structures*, Vol. 77, No. 3, pp. 327–342.

Lu, Y., Ye, L., Wang, D., Wang, X.M. and Su, Z. (2010). "Conjunctive and compromised data fusion schemes for identification of multiple notches in an aluminium plate using Lamb wave signals", *IEEE Transactions on Ultrasonics, Ferroelectrics and Frequency Control*, Vol. 57, No. 9, pp. 2005–2016.

Mayes, R.L. (1992). "Error localization using mode shapes-an application to a two link robot arm", *Proceedings of the Tenth International Modal Analysis Conference*, San Diego, California, USA, pp. 886–891.

Pandey, A.K., Biswas, M. and Samman, M.M. (1991). "Damage detection from changes in curvature mode shapes", *Journal of Sound and Vibration*, Vol. 145, No. 2, pp. 321–332.

Stubbs, N., Kim, J.T. and Topole, K. (1992) "An efficient and robust algorithm for damage localization in offshore platforms", *Proceedings of the Tenth ASCE Structures Congress*, San Antonio, TX, USA, pp. 543–546.

Su, Z., Wang, X., Cheng, L., Yu, L. and Chen, Z. (2009a). "On selection of data fusion schemes for structural damage evaluation", *Structural Health Monitoring*, Vol. 8, No .3, pp. 223–241.

Su, Z., Cheng, L., Wang, X., Yu, L. and Zhou, C. (2009b). "Predicting delamination of composite laminates using imaging approach", *Smart Materials and Structures*, Vol. 18, No. 7.

Xu, H., Cheng, L., Su, Z. and Guyader, J.L. (2011). "Identification of damage in structural components based on locally perturbed dynamic equilibrium", *Journal of Sound and Vibration*, Vol. 330, No. 24, pp. 5963–5981.